Network Controllability in Transmodal Cortex Predicts Positive Psychosis Spectrum Symptoms

Supplementary Information

SUPPLEMENTARY METHODS

Participants

The institutional review boards of both the University of Pennsylvania and the Children's Hospital of Philadelphia approved all study procedures. From the original 1,601 participants from the Philadelphia Neurodevelopmental Cohort (PNC) (1), 156 were excluded due to the presence of gross radiological abnormalities distorting brain anatomy or due to medical history that might impact brain function; those with a history of psychiatric illness were retained. An additional 365 individuals were excluded because they did not pass rigorous manual and automated quality assurance for either their T1-weighted scan or their diffusion scan (2,3). Finally, 12 participants were excluded owing to the presence of disconnected regions in their structural connectivity matrix. This process left a final sample of 1,068 participants. Note that this sample is larger than that commonly reported in previous studies of the PNC dataset (4–6) because, unlike previous reports, we did not exclude based on history of psychiatric illness. Indeed, previous work has illustrated that this broader coverage of the PNC yields prevalence rates of mental disorders consistent with population norms (7).

From the above sample of 1,068, a subsample of 926 participants was used to generate the principal functional gradient (see section titled *Principal gradient of functional connectivity* below) via resting-state functional connectivity analyses (8). These participants met quality control criteria for the resting-state functional magnetic resonance imaging (rs-fMRI) data in the PNC (see section titled *Imaging data quality control* below).

Psychopathology dimensions

In this study, we take a transdiagnostic dimensional approach to assessing variation in the symptoms of mental health (9–12). In particular, we extended a *p-factor* model that was previously developed based on the GOASSESS interview (13,14) and that has previously been used to study the brain (15–17). Briefly, the GOASSESS is an abbreviated and modified structured interview derived from the NIMH Genetic Epidemiology Research Branch Kiddie-SADS (18) that covers a wide variety of psychiatric symptomatology such as the occurrence of mood (major depressive episode, mania), anxiety (agoraphobia, generalized anxiety, panic, specific phobia, social phobia, separation anxiety, obsessive compulsive disorder), externalizing behavior (oppositional defiant, attention deficit/hyperactivity, conduct disorder), eating disorder (anorexia, bulimia), and suicidal thoughts and behaviors. GOASSESS was administered by trained and certified assessors. The original model used a combination of exploratory and confirmatory factor analysis to distill the 112 item-level symptoms from the GOASSESS into five orthogonal dimensions of psychopathology. The original model included a factor common to all psychiatric disorders, referred to as overall psychopathology, as well as four specific factors: anxious-misery, psychosis, externalizing behaviors, and fear.

Here, owing to emergent evidence that the positive and negative aspects of the psychosis spectrum elicit unique effects on the brain (19), we extended the above *p-factor* model in two ways. First, we included an additional five assessor-rated polytomous items (scored from 0-6, where 0 is 'absent' and 6 is 'severe and psychotic' or 'extreme' from the Scale of Prodromal Symptoms (SOPS) derived from the Structured Interview for Prodromal Syndromes (SIPS (20)) designed to measure the negative/disorganized symptoms of psychosis. These five items were (i) P5 disorganized communication, (ii) N2 avolition, (iii) N3 expression of emotion, (iv) N4 experience of emotions and self, and (v) N6 occupational functioning. Including this additional set brought the total to 117 items. Second, we split the psychosis factor into two factors, one describing the delusions and hallucinations associated with the psychosis spectrum, which we call psychosis-positive. The second psychosis factor described disorganized thought, cognitive impairments, and motivational-emotional deficits, which we call psychosis-negative for simplicity. We used confirmatory factor analysis implemented in Mplus (21) to model five specific factors of psychopathology (anxious-misery, psychosis-positive, psychosis-negative, externalizing behaviors, and fear) as well as one common factor (overall psychopathology). Note that all dimensions derived from this model are orthogonal to one another. Here, we primarily studied the psychosis-positive and psychosis-negative dimensions, which represent the positive and negative domains of the PS, respectively (22). We also studied the overall psychopathology dimension.

Imaging data acquisition

MRI data were acquired on a 3 Tesla Siemens Tim Trio scanner with a 32-channel head coil at the Hospital of the University of Pennsylvania. Diffusion tensor imaging (DTI) scans were acquired via a twice-refocused spin-echo (TRSE) single-shot echo-planar imaging (EPI) sequence (TR = 8100 ms, TE = 82 ms, FOV = 240mm^2/240mm^2; Matrix = RL: 128, AP: 128, Slices: 70, in-plane resolution of 1.875mm^2; slice thickness = 2mm, gap = 0; flip angle = 90°/180°/180°, 71 volumes, GRAPPA factor = 3, bandwidth = 2170 Hz/pixel, PE direction = AP). Our sequence utilized a four-lobed diffusion encoding gradient scheme combined with a 90-180-180 spin-echo sequence designed to minimize eddy-current artifacts (1). The sequence consisted of 64 diffusion-weighted directions with $b = 1000$ s/mm^2 and 7 interspersed scans where $b = 0$ s/mm^2. The imaging volume was prescribed in axial orientation and covered the entire brain.

In addition to the DTI scan, a B0 map of the main magnetic field was derived from a double-echo, gradient-recalled echo (GRE) sequence, allowing for the estimation and correction of field distortions. Prior to DTI acquisition, a 5-min magnetization-prepared, rapid acquisition gradient-echo T1-weighted (MPRAGE) image (TR = 1810ms, TE = 3.51ms, FOV = 180 x 240mm, matrix 256 x 192, voxel resolution of 1mm^3) was acquired for each participant.

Finally, approximately 6 minutes of rs-fMRI data was acquired using a blood oxygen level-dependent (BOLD-weighted) sequence (TR = 3000ms; TE = 32ms; FoV = 192 x 192mm; resolution 3mm isotropic; 124 volumes). These data were used solely to generate the principal cortical gradient of functional connectivity discussed in the main text (8).

Imaging data quality control

All DTI and T1-weighted images underwent rigorous quality control by highly trained image analysts (see Refs. (2) and (3) for details on DTI and T1-weighted imaging, respectively). Regarding the DTI acquisition, all 71 volumes were visually inspected and evaluated for the presence of artifacts. Every volume with an artifact was marked as contaminated and the fraction of contaminated volumes was taken as an index of scan quality. Scans were marked as ‘poor’ if more than 20% of volumes were contaminated, ‘good’ if more than 0% but less 20% of volumes were contaminated, and ‘great’ if 0% of volumes were contaminated. Regarding the T1-weighted acquisition, images with gross artifacts were considered unusable; images with some artifacts were flagged as ‘decent’; and images free of artifact were marked as ‘superior’. As mentioned above in the section titled *Participants*, 365 individuals were removed due to either ‘poor’ diffusion tensor images or ‘unusable’ T1-weighted images. In the main sample of 1,068, a total of 655 participants had diffusion tensor images identified as ‘great’, with the remaining identified as ‘good’, and 924 participants had T1-weighted images identified as ‘superior’, with the remaining identified as ‘usable’. Regarding the rs-fMRI data, as in prior work (23,24), a participant’s rs-fMRI run was excluded if the mean relative root mean square (RMS) framewise displacement was higher than 0.2mm, or it had more than 20 frames with motion exceeding 0.25mm.

Structural image processing

Structural image processing was carried out using tools included in ANTs (25). The buildtemplateparallel pipeline from ANTs (26) was used to create a study-specific T1-weighted structural template with 120 participants that were balanced on sex, race, and age. Structural images were processed in participant’s native space using the following procedure: brain extraction, N4 bias field correction (27), Atropos tissue segmentation (28), and SyN diffeomorphic registration (26,29).

Diffusion image processing

For each participant, a binary mask was created by registering the standard fractional anisotropy mask provided by FSL (FMRIB58 FA) to the participant's mean b=0 reference image using FLIRT (30). To correct for eddy currents and head motion, this mask and the participant's diffusion acquisition was passed to FSL's *eddy* (31) (version 5.0.5). Diffusion gradient vectors were subsequently rotated to adjust for the motion estimated by *eddy*. Distortion correction was conducted via FSL's FUGUE (32) using the participant's field map, estimated from the b=0 map.

For each subject, whole-brain deterministic fiber tracking was conducted using DSI Studio (33) with a modified fiber assessment by continuous tracking (FACT) algorithm with Euler interpolation. A total of 1,000,000 streamlines were generated for each participant that were between 10mm and 400mm long. Fiber tracking was performed with an angular threshold of 45° and step size of 0.9375mm. For each subject, the number of streamlines intersecting region i and region j in a given parcellation (see section entitled *Whole brain parcellation* below) was used to weight the edges of an undirected adjacency matrix, $\boldsymbol{A}$. Note, $\boldsymbol{A}_{ij} = 0$ for $i = j$.

Limitations of tractography

Tractography has limitations when it comes to measuring structural connectivity. Tractography is insensitive to both the directionality of, and the synaptic processes occurring along, white matter pathways. In our study, Network Control Theory assumes that signals originating at a given region propagate throughout the network based on the strength of inter-regional connectivity alone. Thus, in our model, insensitivity to directionality means that signals can traverse from one region to the next along both efferent and afferent connections equally, instead of being constrained to the efferent connections. Indeed, insensitivity to directionality may explain some of the divergence often observed between white matter paths derived from diffusion tractography and those derived from non-human tract-tracing experiments (34,35). However, we note that prior work has shown that controllability statistics generated from directional tract-tracing data are similar to those derived from undirected data (36). Additionally, similar to previous work (37), we make the assumption that two regions not connected directly can communicate with each other polysynaptically via an intermediate region. However, without sensitivity to what is occurring at synapses, we are unable to determine whether signals that arrive at an intermediate region actually propagate along downstream connections or not. While there is evidence that regional strength (derived from diffusion tractography) correlates to comparable regional summaries of tract-tracing connectivity (38,39), this effect only accounts for direct connections. It remains unclear how, and to what extent, measures of indirect connectivity, like those studied herein (e.g., average controllability), relate to summaries of tract-tracing connectivity that account for polysynaptic processes (40). Despite these limitations, diffusion-weighted tractography remains the only way to index structural connectivity *in vivo*, which is essential to studying how inter-individual differences in the human brain link to PS symptoms throughout development.

rs-fMRI processing

State-of-the-art processing of functional data is critical for valid inference (41). Thus, functional images were processed using a top-performing preprocessing pipeline implemented using the eXtensible Connectivity Pipeline (XCP) Engine (24), which includes tools from FSL (32,42) and AFNI (43). This pipeline included (1) correction for distortions induced by magnetic field inhomogeneity using FSL's FUGUE utility, (2) removal of 4 initial volumes, (3) realignment of all volumes to a selected reference volume using FSL's MCFLIRT, (4) interpolation of intensity outliers in each voxel's time series using AFNI's 3dDespike utility, (5) demeaning and removal of any linear or quadratic trends, and (6) co-registration of functional data to the high-resolution structural image using boundary-based registration. Images were de-noised using a 36-parameter confound regression model that has been shown to minimize associations with motion artifact while retaining signals of interest in distinct sub-networks (24,41,44). This model included the six framewise estimates of motion, the mean signal extracted from eroded white matter and cerebrospinal fluid compartments, the mean signal extracted from the entire brain, the derivatives of each of these nine parameters, and quadratic terms of each of the nine parameters and their derivatives. Both the BOLD-weighted time series and the artifactual model time series were temporally filtered using a first-order Butterworth filter with a passband between 0.01 and 0.08 Hz (45).

Whole brain parcellation

Studying whole-brain connectivity with neuroimaging data requires the separation of the brain into discrete regions via the use of a parcellation. Here, we primarily adopted a 200-region parcellation defined in a previous study by Schaefer *et al.* (46) using functional neuroimaging data; this parcellation is hereafter referred as the Schaefer200 parcellation. Our decision to adopt a functionally-defined parcellation to study structural connectivity was motivated by our goal to contextualize our predictive analyses against the functional cortical hierarchy (8). This choice is also consistent with our previous work that examined the coupling between structural and functional connectivity in the PNC (47). However, there exist a plethora of brain parcellations that vary both in their nature and in their spatial resolution. In light of this diversity, we repeated our analyses using three additional parcellations of the brain. First, we used a higher resolution version of the Schaefer parcellation that included 400 regions covering the cortex (Schaefer400). Second, we used a parcellation wherein boundaries were defined according to neuroanatomy rather than function and that included 234 regions covering the cortex and subcortex (Lausanne234) (48). Third, we used a multi-modal parcellation developed in the Human Connectome Project data that included 360 regions covering the cortex (HCP-MMP) (49).

Alternative graph-theoretic measures of indirect connectivity

As mentioned in the main text, average controllability is not the only way to probe indirect connections to a region. In order to examine the extent to which our analyses of individual differences were specific to average controllability, we included three additional graph-theoretic measures of centrality that also characterize indirect connections to a region (50), albeit in the absence of a dynamical model. These metrics were: (i) betweenness centrality, (ii) closeness centrality, (iii) and subgraph centrality. For extended discussion and definition of these metrics, we refer the interested reader to previous work by Oldham *et al.* (50). Briefly, betweenness centrality represents the extent to which a region is situated along shortest paths that link together other pairs of regions; a region with a high betweenness centrality value lies along more of these paths than a region with a low betweenness centrality value. Closeness centrality is the average of the shortest path lengths that run from a region to all other reachable regions in the network; a region with a high closeness centrality value has lower average shortest paths to other areas than a region with a low closeness centrality. Finally, a region with high subgraph centrality is involved in many closed walks (i.e., paths that begin and end at the same region). Together, these centrality metrics cover a broad spectrum of how indirect connections can influence a region, including paths that run through a region, paths that originate at a region, and paths that begin and end at a region.

Nuisance covariates

In this study, we used age, sex (binary), total brain volume, and mean in-scanner motion as nuisance covariates. Total brain volume was generated from the T1-weighted images using ANTs. In-scanner head motion was estimated for each participant from their diffusion sequence as relative framewise displacement (2). Specifically, rigid-body motion correction was applied to the seven high quality $b = 0$ images interspersed throughout the diffusion acquisition. Once estimated, framewise displacement was averaged across time to create a single measure for each participant (see Figure S5).

Machine learning prediction models

As discussed in the main text, we generated five $1{,}068 \times 200$ matrices (X) of regional structural connectivity features — strength (X_s), average controllability (X_a), betweenness centrality (X_{bc}), closeness centrality (X_{cc}), and subgraph centrality (X_{sgc}) — that were used to iteratively predict symptom dimensions (y) in a series of prediction models. Here, we describe these models in greater detail, including our use and comparison of both linear and nonlinear regression estimators ($regr$) (see Figures S6 and S7 for results).

Primary prediction model

In order to elucidate whether the link between connectivity features (X) and symptom dimensions (y) was linear or nonlinear, we used both linear ridge regression (RR) and kernel ridge regression (KRR) with a radial basis function (51). Regression estimators were fit using *scikit-learn* (52) with default parameters (RR: $\alpha = 1$; KRR: $\alpha = 1, \gamma = 1/n$, where n represents the number of brain regions). For each $(regr, X, y)$ combination, we assessed out-of-sample prediction performance using 10-fold cross-validation scored by root mean squared error (RMSE) and the correlation between the true y and predicted y. Note, because symptom dimensions were standardized prior to prediction analysis as part of normalization, RMSE was consequently standardized such that values of <1 were within 1 standard deviation of y. Models were trained using all columns of a given X matrix as input features and RMSE and the correlation between the true y and predicted y were each averaged across folds. We included age, sex, total brain volume, and in-scanner motion as nuisance covariates (see section titled *Nuisance covariates* above). All nuisance covariates, except for sex, were normalized using an inverse normal transformation. Nuisance covariates were controlled for by regressing their effect out of X before predicting y. Within each fold, nuisance covariates were fit to the training data and applied to the test data to prevent leakage. Next, owing to evidence that prediction performance can be biased by the arbitrariness of a single split of the data (53), we repeated 10-fold cross-validation 100 times, each time with a different random 10-fold split. Together, this process yielded a distribution of 100 mean RMSE values and 100 mean correlations between true y and predicted y for each $(regr, X, y)$ combination. Schematic illustration of our *primary prediction model* is presented in Figure 1B in the main text. For each symptom dimension (y), we compared prediction performance (e.g., RMSE distributions) across pairs of connectivity features (e.g., X_s versus X_a) using an exact test of differences (54).

Secondary prediction model

Our primary prediction model did not perform hyper-parameter optimization, instead relying on default settings for both regression estimators ($\alpha = 1$). This decision was motivated by our desire to incorporate nuisance covariates into our prediction model while minimizing leakage; a problem that may spuriously improve prediction performance (55). While *scikit-learn* includes tools for conducting unbiased hyper-parameter optimization via nested cross-validation (53), it is not set up to do both nested cross-validation and leakage-resistant nuisance regression concurrently. As such, we specified a *secondary prediction model* that did not include nuisance regression and instead performed hyper-parameter (α) optimization via 10-fold nested cross-validation (Figure S1). Specifically, for each fold of the test data, the remaining training data was once more subjected to 10-fold cross-validation in order to find the best performing α parameter (i.e., inner-loop cross-validation). The optimal α parameter from this inner loop was then fit to the full training data and used to predict the test data. This approach isolates the evaluation of model performance from the optimization of α. As above, prediction performance was compared across pairs of connectivity features (e.g., X_s versus X_a) using an exact test of differences (54).

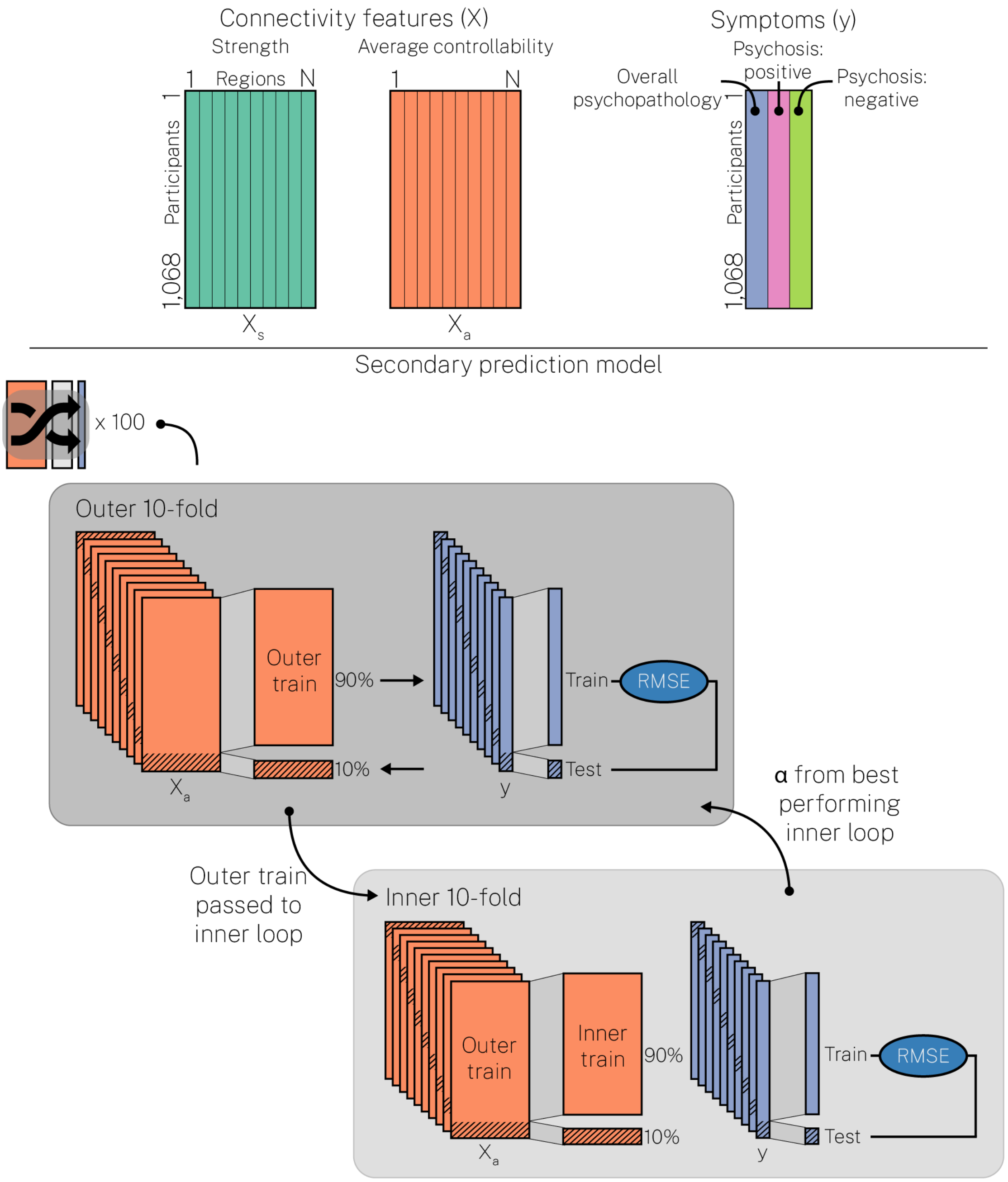

Figure S1. Secondary prediction model. The variable X (e.g., strength, X_s; average controllability, X_a) was used to predict y via 100 repeats of *nested* 10-fold cross-validation; each repeat used a different random split of the data. Hyper-parameters were optimized in the inner-loop and the best performing hyper-parameter was fed back to the outer-loop to assess performance on the test set.

Null prediction model

Both our primary and secondary prediction models generated robust estimates of prediction performance for a given (reg, X, y) combination but they did not examine whether prediction performance was in itself significant. Thus, in order to test whether prediction performance was better than chance, we compared point estimates of each of our scoring metrics (e.g., RMSE) to the distribution of values obtained from permuted data. Specifically, we trained each $(regr, X, y)$ combination on a single cross-validation split, stratified on y, and then subjected the corresponding point estimates to 100,000 random permutations, wherein the rows (i.e., participants) of y were randomly shuffled. The associated p-values were assigned as the proportion of permuted scores that were greater than or equal to our true scores and corrected for multiple comparisons over connectivity features and symptom dimensions (5 x 3 = 15 tests) via the Benjamini and Hochberg False Discovery Rate (FDR, $q = 0.05$) procedure (56). We refer to this model as our *null prediction model* (Figure S2). Note, as per *scikit-learn* defaults, for RMSE, models were trained and evaluated using a negative sign so as to ensure that greater RMSE corresponded to better performance. This, in turn, ensured that p-values were computed correctly using the above procedure. However, for ease of interpretation, we present unsigned RMSE throughout the results.

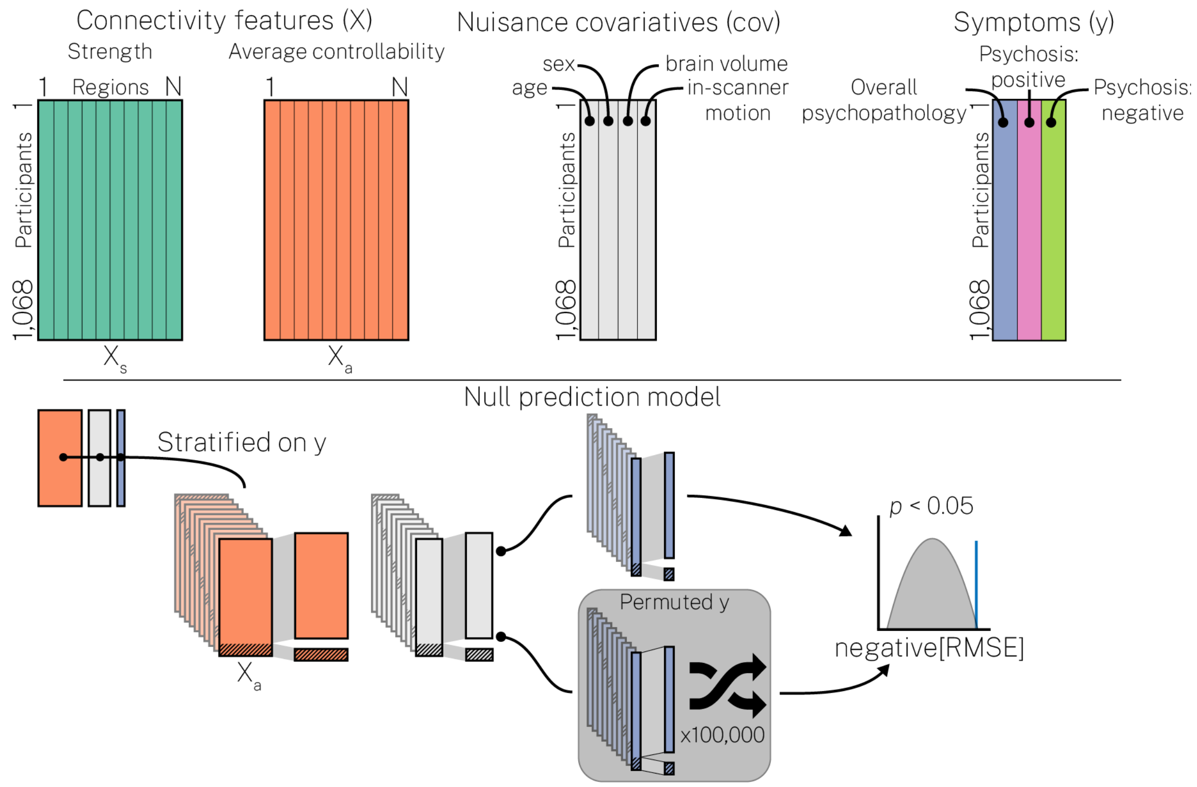

Figure S2. Null prediction model. The variable X (e.g., strength, X_s; average controllability, X_a) was used to predict y, controlling for age, sex, brain volume, and in-scanner motion, via a single split of the data stratified on y. This model was subjected to 100,000 random permutations (of y) to test for statistical significance.

Binned-regions prediction model

Finally, the KRR prediction estimator that we used above was nonlinear, which meant we were unable to extract interpretable regional coefficients from our prediction models when using this estimator. Thus, we sought an approach to examining each region’s contribution to prediction performance that was agnostic to the nonlinear nature of our KRR. As above, we trained a given (X, y) combination on a single cross-validation split, stratified on y. However, instead of training on all columns of X, we trained on non-overlapping subsets of five columns sampled along the principal cortical gradient of functional connectivity (8). The principal cortical gradient separates the transmodal cortex from unimodal cortex in a continuous fashion, which allowed us to characterize gradual changes in prediction performance of each connectivity feature as a function of the cortical hierarchy. We derived the cortical gradient in our own data (see section entitled *Principal gradient of functional connectivity* below). As above, we assessed prediction significance using a permutation test, wherein the rows of y were randomly shuffled 100,000 times. Empirical nulls were generated separately for each bin of five regions. We refer to this final model as our *binned-regions prediction model* (Figure 1C).

Principal gradient of functional connectivity

Here, we characterized whole-brain resting-state functional connectivity according to a gradient that situates unimodal sensorimotor cortex at one end and transmodal association cortex at the other. The details of this approach are explained in prior work by Margulies *et al.* (8). Conceptually, this approach amounts to a dimensionality reduction technique that positions regions with similar functional connectivity profiles near to one another and distant from those with dissimilar connectivity profiles. Here, for each participant, processed rs-fMRI timeseries (see section titled *rs-fMRI processing* above) were averaged regionally and regional timeseries were correlated pairwise to generate functional connectomes. Correlations were estimated via Pearson's correlation coefficient and connectomes were normalized using Fisher's r-to-z transform before being averaged over participants. The principal cortical gradient was generated from this group-average connectome with the *BrainSpace* toolbox (57), using the *DiffusionMaps* approach and *normalized_angle* kernel. We selected the first gradient output from this approach, which closely aligned to that observed by Margulies *et al.* (8) (see Figure 3 in the main text). Thus, this process resulted in a 200×1 vector for the Schaefer200 that described each region's position along the principal gradient.

Varying the contribution of indirect connectivity to average controllability

In the main text, we discussed the normalization of participant's $\boldsymbol{A}$ matrices (*Eq. 3*) prior to estimating average controllability (*Eq. 4*). Increasing the c parameter from 1 (default) to 10000 increases the rate of decay of the system, causing the system to stabilize at zero (i.e., no activity) more rapidly (58). It follows that energy distributed from a region of interest (i.e., average controllability) will be limited in its capacity to spread throughout a fast-decaying system compared to a (relatively) slow-decaying system. In turn, we reasoned that increasing c would increasingly restrict average controllability's capacity to access indirect aspects of regional structural connectivity profiles, limiting the spread of activity beyond direct connections.

Here, in the Supplement, we illustrate the effect of tuning c using a simple toy network. In particular, we define a toy network of 5 regions with randomly generated connection weights (Figure S3A). Then, we use this network to simulate the spread of activity from a single region of interest. We repeated this simulation to test the impact of (i) lesioning indirect connections (Figure S3B) and (ii) varying the c parameter [1 (default), 10, 100, 1000, 10000] (Figure S3C). For the former, lesioning involved turning off the connection weights of edges that were not directly connected to our region of interest (i.e., the indirect connections). All code to reproduce these simulations can be found on the first author's GitHub page: https://github.com/lindenmp/linear_system_demos/blob/master/impulse_response.ipynb.

Figure S3B shows that average controllability diminished as we lesioned stronger indirect connections. Note, because all direct connections remained intact, strength is by definition unaffected. Next, Figure S3C (top) shows that activity spread the furthest throughout the toy network when $c = 1$. Moreover, average activity (over nodes) diminished to zero more rapidly over time at higher c (Figure S3C, bottom). Together, these simulations demonstrate how average controllability is sensitive to the indirect connections to a region, and that increasing c limits average controllability's capacity to access these properties. As such, in the main text, we examined the impact of varying the c parameter on prediction performance by repeating our binned-regions prediction model (Figure 1C) for each of the aforementioned values of c.

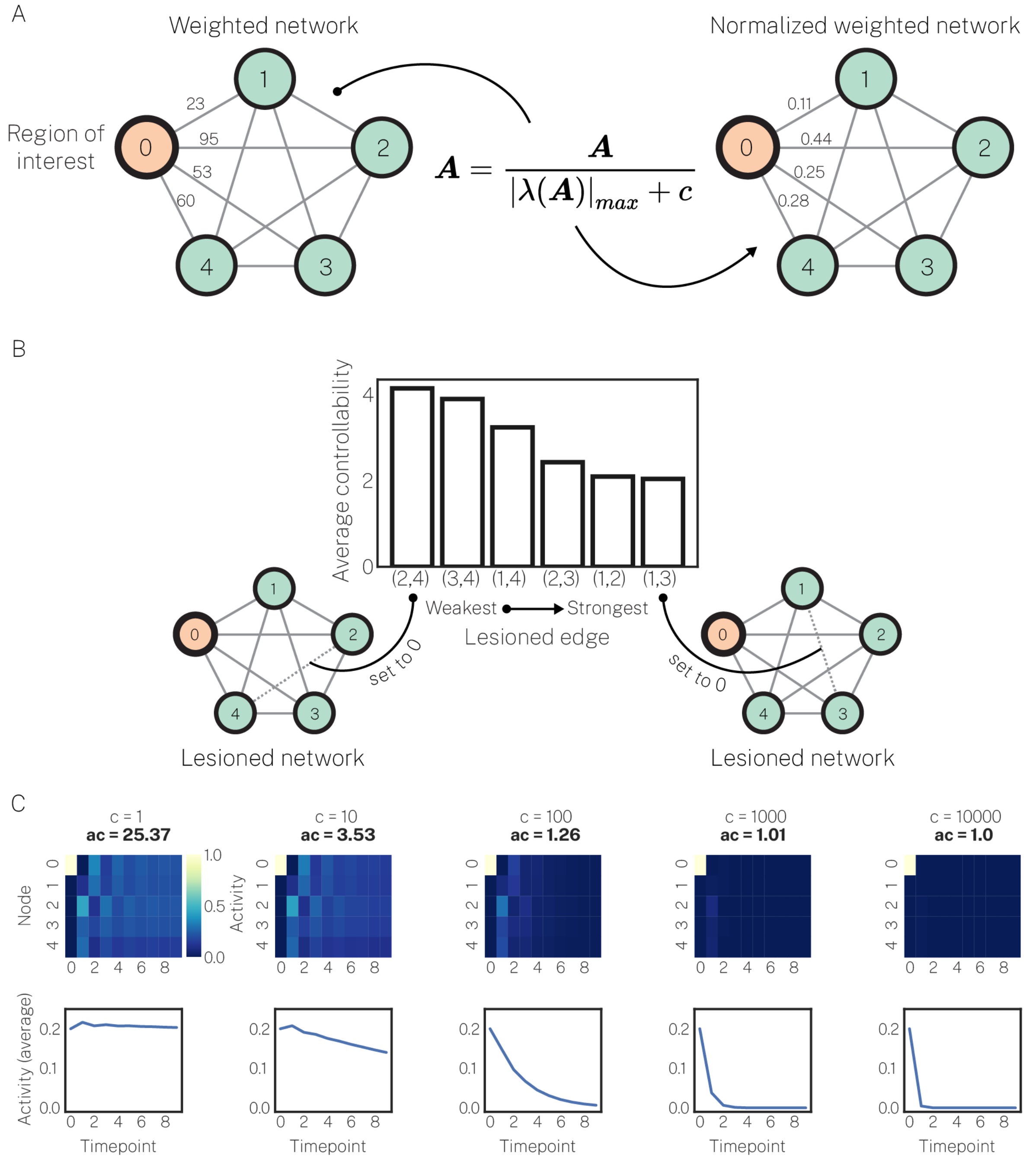

Figure S3. Simulating the linear dynamical system and manipulating the normalization parameter (*c*). A, A fully connected and weighted toy network comprising 5 regions was used to simulate the linear dynamical system. While all edges were weighted, only the direct connections to our region of interest are illustrated for simplicity. **B**, Average controllability was calculated for this region of interest multiple times, each time lesioning one of the indirect connections from the region of interest. Lesioning the strongest indirect connections yielded the smallest estimate of average controllability. Note that the direct connections were never lesioned in this analysis. **C**, Using the full network, we simulated the linear system over a restricted set of time steps (n=10) as a function of increasing c (columns). The top row shows activity at each region at each timepoint, represented as a heatmap. The bottom row shows activity averaged over regions at each timepoint. Greater values of c caused the spread of activity to diminish to 0 increasingly quickly. This decreased activity spread corresponded to a reduction in average controllability (ac) from 25.37 to 1.0. Note that average controllability at $c = 1$ is high (25.47) owing to the size and fully connected nature of the toy network. Once a single connection is lesioned, average controllability drops dramatically.

SUPPLEMENTARY RESULTS

Dimensional measures of the psychosis spectrum

Males in our sample had significantly higher psychosis-positive ($t = 2.34$, $p < 0.05_{FDR}$) and psychosis-negative ($t = 3.41$, $p < 0.05_{FDR}$) scores compared to females. Age correlated significantly with higher overall psychopathology ($r = 0.29$, $p < 0.05_{FDR}$) and lower psychosis-positive ($r = -0.09$, $p < 0.05_{FDR}$) scores. Below we illustrate model statistics (Table S1) and factor loadings (Table S2) for our bifactor model of psychopathology from which positive and negative PS symptoms were extracted.

Table S1. Factor determinacy and Omega-H scores for bifactor model of psychopathology dimensions.

Item	General (‘*p*’)	Psychosis-positive	Psychosis-negative	Anxious-misery	Externalizing	Fear
Factor determinacy	0.9927	0.9600	0.9683	0.9548	0.9661	0.9502
$\text{OmegaH}_{\text{subscale}}$	0.9213	0.0154	0.0056	0.0004	0.0276	0.0192

Table S2. Factor loadings from bifactor model of psychopathology dimensions.

	Loadings					
Item	General (‘*p*’)	Psychosis-positive	Psychosis-negative	Anxious-misery	Externalizing	Fear
psy001	**0.657**	**0.442**	0.000	0.000	0.000	0.000
psy029	**0.606**	**0.411**	0.000	0.000	0.000	0.000
psy050	**0.632**	**0.220**	0.000	0.000	0.000	0.000
psy060	**0.666**	**0.316**	0.000	0.000	0.000	0.000
psy070	**0.637**	**0.285**	0.000	0.000	0.000	0.000
psy071	**0.721**	**0.187**	0.000	0.000	0.000	0.000
sip003	**0.598**	**0.522**	0.000	0.000	0.000	0.000
sip004	**0.422**	**0.616**	0.000	0.000	0.000	0.000
sip005	**0.593**	**0.605**	0.000	0.000	0.000	0.000
sip006	**0.557**	**0.559**	0.000	0.000	0.000	0.000
sip007	**0.584**	**0.608**	0.000	0.000	0.000	0.000
sip008	**0.519**	**0.628**	0.000	0.000	0.000	0.000
sip009	**0.615**	**0.502**	0.000	0.000	0.000	0.000
sip010	**0.437**	**0.666**	0.000	0.000	0.000	0.000
sip011	**0.623**	**0.607**	0.000	0.000	0.000	0.000
sip012	**0.639**	**0.596**	0.000	0.000	0.000	0.000
sip013	**0.605**	**0.593**	0.000	0.000	0.000	0.000
sip014	**0.715**	**0.489**	0.000	0.000	0.000	0.000
sip027	**0.487**	0.000	**0.288**	0.000	0.000	0.000
sip028	**0.517**	0.000	**0.305**	0.000	0.000	0.000
sip032	**0.758**	0.000	**0.188**	0.000	0.000	0.000

sip033	**0.681**	0.000	**0.205**	0.000	0.000	0.000
sip038	**0.396**	0.000	**0.795**	0.000	0.000	0.000
sip039	**0.483**	0.000	**0.631**	0.000	0.000	0.000
SIP030	**0.524**	0.000	**0.383**	0.000	0.000	0.000
SIP035	**0.714**	0.000	**0.302**	0.000	0.000	0.000
SIP037	**0.387**	0.000	**0.395**	0.000	0.000	0.000
SIP041	**0.459**	0.000	**0.846**	0.000	0.000	0.000
SIP043	**0.496**	0.000	**0.678**	0.000	0.000	0.000
SIP001	**0.461**	0.000	**0.328**	0.000	0.000	0.000
add011	**0.473**	0.000	0.000	0.000	**0.745**	0.000
add012	**0.458**	0.000	0.000	0.000	**0.749**	0.000
add013	**0.490**	0.000	0.000	0.000	**0.596**	0.000
add014	**0.442**	0.000	0.000	0.000	**0.606**	0.000
add015	**0.499**	0.000	0.000	0.000	**0.565**	0.000
add016	**0.510**	0.000	0.000	0.000	**0.678**	0.000
add020	**0.497**	0.000	0.000	0.000	**0.543**	0.000
add021	**0.448**	0.000	0.000	0.000	**0.599**	0.000
add022	**0.468**	0.000	0.000	0.000	**0.603**	0.000
agr001	**0.611**	0.000	0.000	0.000	0.000	**0.474**
agr002	**0.635**	0.000	0.000	0.000	0.000	**0.489**
agr003	**0.651**	0.000	0.000	0.000	0.000	**0.421**
agr004	**0.550**	0.000	0.000	0.000	0.000	**0.422**
agr005	**0.523**	0.000	0.000	0.000	0.000	**0.469**
agr006	**0.620**	0.000	0.000	0.000	0.000	**0.457**
agr007	**0.621**	0.000	0.000	0.000	0.000	**0.286**
agr008	**0.621**	0.000	0.000	0.000	0.000	**0.453**
cdd001	**0.573**	0.000	0.000	0.000	**0.407**	0.000
cdd002	**0.548**	0.000	0.000	0.000	**0.219**	0.000
cdd003	**0.621**	0.000	0.000	0.000	**0.462**	0.000
cdd004	**0.468**	0.000	0.000	0.000	**0.334**	0.000
cdd005	**0.606**	0.000	0.000	0.000	**0.477**	0.000
cdd006	**0.613**	0.000	0.000	0.000	**0.384**	0.000
cdd007	**0.635**	0.000	0.000	0.000	**0.372**	0.000
cdd008	**0.637**	0.000	0.000	0.000	**0.348**	0.000
dep001	**0.760**	0.000	0.000	**0.220**	0.000	0.000
dep002	**0.724**	0.000	0.000	**0.187**	0.000	0.000
dep004	**0.791**	0.000	0.000	**0.031**	0.000	0.000
dep006	**0.775**	0.000	0.000	**0.034**	0.000	0.000
gad001	**0.506**	0.000	0.000	**0.377**	0.000	0.000
gad002	**0.554**	0.000	0.000	**0.404**	0.000	0.000
man001	**0.743**	0.000	0.000	**-0.517**	0.000	0.000
man002	**0.744**	0.000	0.000	**-0.567**	0.000	0.000
man003	**0.732**	0.000	0.000	**-0.523**	0.000	0.000
man004	**0.771**	0.000	0.000	**-0.456**	0.000	0.000
man005	**0.767**	0.000	0.000	**-0.460**	0.000	0.000

man006	**0.689**	0.000	0.000	**-0.487**	0.000	0.000
man007	**0.808**	0.000	0.000	**-0.241**	0.000	0.000
ocd001	**0.844**	0.000	0.000	**0.197**	0.000	0.000
ocd002	**0.807**	0.000	0.000	**0.125**	0.000	0.000
ocd003	**0.709**	0.000	0.000	**0.209**	0.000	0.000
ocd004	**0.826**	0.000	0.000	**0.060**	0.000	0.000
ocd005	**0.822**	0.000	0.000	**0.115**	0.000	0.000
ocd006	**0.843**	0.000	0.000	**0.107**	0.000	0.000
ocd007	**0.665**	0.000	0.000	**0.143**	0.000	0.000
ocd008	**0.766**	0.000	0.000	**0.131**	0.000	0.000
ocd011	**0.712**	0.000	0.000	**0.196**	0.000	0.000
ocd012	**0.721**	0.000	0.000	**0.134**	0.000	0.000
ocd013	**0.699**	0.000	0.000	**0.119**	0.000	0.000
ocd014	**0.763**	0.000	0.000	**0.061**	0.000	0.000
ocd015	**0.732**	0.000	0.000	**0.092**	0.000	0.000
ocd016	**0.714**	0.000	0.000	**0.150**	0.000	0.000
ocd017	**0.719**	0.000	0.000	**0.090**	0.000	0.000
ocd018	**0.629**	0.000	0.000	**0.095**	0.000	0.000
ocd019	**0.561**	0.000	0.000	**0.073**	0.000	0.000
odd001	**0.588**	0.000	0.000	0.000	**0.436**	0.000
odd002	**0.573**	0.000	0.000	0.000	**0.515**	0.000
odd003	**0.532**	0.000	0.000	0.000	**0.568**	0.000
odd005	**0.553**	0.000	0.000	0.000	**0.486**	0.000
odd006	**0.634**	0.000	0.000	0.000	**0.397**	0.000
pan001	**0.621**	0.000	0.000	**0.275**	0.000	0.000
pan003	**0.692**	0.000	0.000	**0.156**	0.000	0.000
pan004	**0.779**	0.000	0.000	**0.159**	0.000	0.000
phb001	**0.276**	0.000	0.000	0.000	0.000	**0.309**
phb002	**0.340**	0.000	0.000	0.000	0.000	**0.350**
phb003	**0.422**	0.000	0.000	0.000	0.000	**0.282**
phb004	**0.270**	0.000	0.000	0.000	0.000	**0.355**
phb005	**0.186**	0.000	0.000	0.000	0.000	**0.263**
phb006	**0.456**	0.000	0.000	0.000	0.000	**0.314**
phb007	**0.418**	0.000	0.000	0.000	0.000	**0.388**
phb008	**0.365**	0.000	0.000	0.000	0.000	**0.199**
scr001	**0.494**	0.000	0.000	0.000	**0.163**	0.000
scr006	**0.487**	0.000	0.000	0.000	**0.357**	0.000
scr007	**0.651**	0.000	0.000	**0.210**	0.000	0.000
scr008	**0.545**	0.000	0.000	0.000	**0.255**	0.000
sep500	**0.462**	0.000	0.000	0.000	0.000	**0.168**
sep508	**0.413**	0.000	0.000	0.000	0.000	**0.202**
sep509	**0.433**	0.000	0.000	0.000	0.000	**0.226**
sep510	**0.525**	0.000	0.000	**0.085**	0.000	0.000
sep511	**0.310**	0.000	0.000	0.000	0.000	**0.108**
soc001	**0.444**	0.000	0.000	0.000	0.000	**0.638**

soc002	**0.436**	0.000	0.000	0.000	0.000	**0.557**
soc003	**0.383**	0.000	0.000	0.000	0.000	**0.708**
soc004	**0.449**	0.000	0.000	0.000	0.000	**0.685**
soc005	**0.486**	0.000	0.000	0.000	0.000	**0.661**
sui001	**0.647**	0.000	0.000	**0.185**	0.000	0.000
sui002	**0.740**	0.000	0.000	**0.260**	0.000	0.000

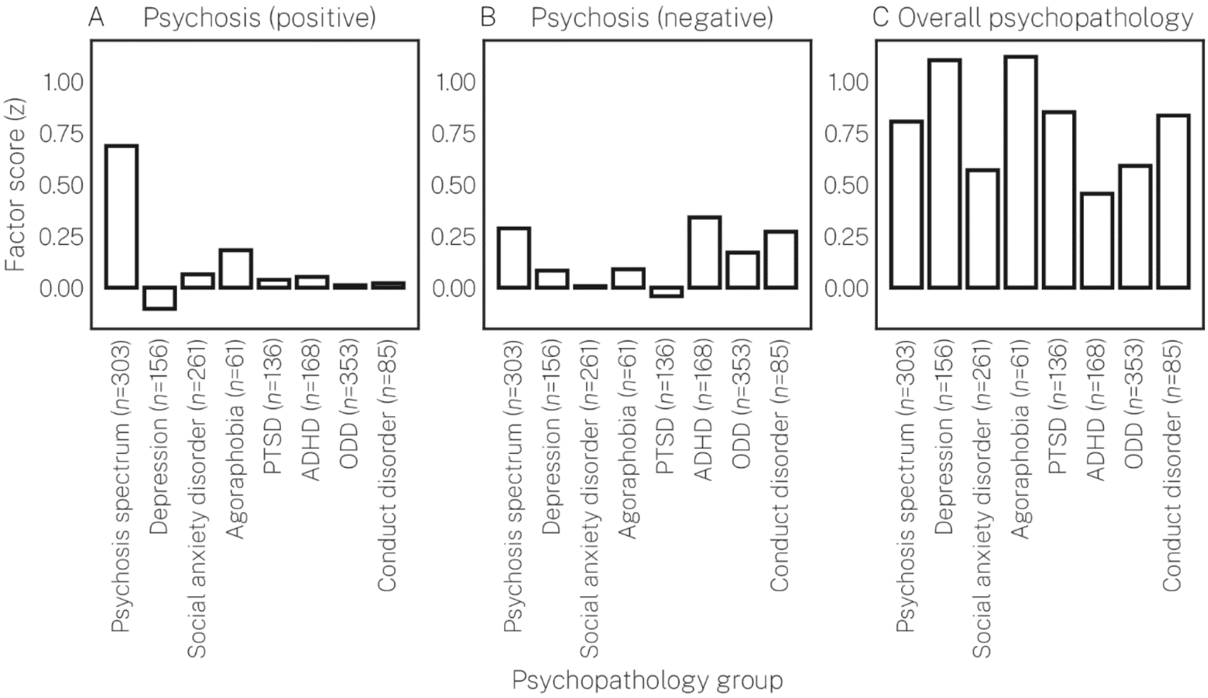

Figure S4. Mean psychopathology symptom dimensions as a function of psychopathology groups. Groups are the same as those presented in Table 1 in the main text. Only groups where *n*≥50 are shown here.

In-scanner motion

In Figure S5 we report the distribution of our estimate of in-scanner motion, which was used as a nuisance covariate in our predictive models (see the section entitled *Machine learning prediction models* in the main text). In-scanner motion was estimated as the mean over relative framewise displacement values derived from rigid-body motion correction applied to each participant's DTI scan (see Roalf *et al.*, (2) for details).

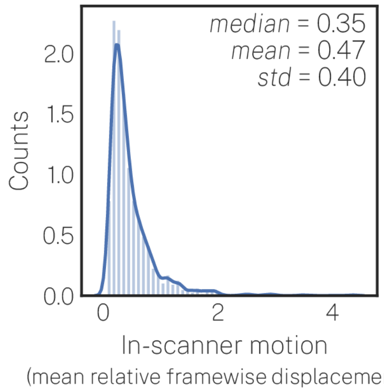

Figure S5. Descriptive statistics for in-scanner motion from participants' DTI scans. Distribution of in-scanner motion over participants estimated as the mean over relative framewise displacement values. For each DTI scan, relative framewise displacement was calculated by rigid-body motion correction. In-scanner motion was used a nuisance covariate in all prediction models.

Nonlinear regression outperforms linear regression in predicting psychosis symptoms

We sought to determine whether the mapping from structural connectivity features to symptom dimensions was best characterized by nonlinear or linear regression functions. For both our *primary prediction model* (Figure S6; nuisance regression without hyper-parameter optimization), and *secondary prediction model* (Figure S7; hyper-parameter optimization without nuisance regression), kernel ridge regression (KRR) unambiguously outperformed ridge regression (RR) for all combinations of connectivity features and symptom dimensions. Given this unequivocal result, KRR was used as the sole regression estimator in all subsequent analyses.

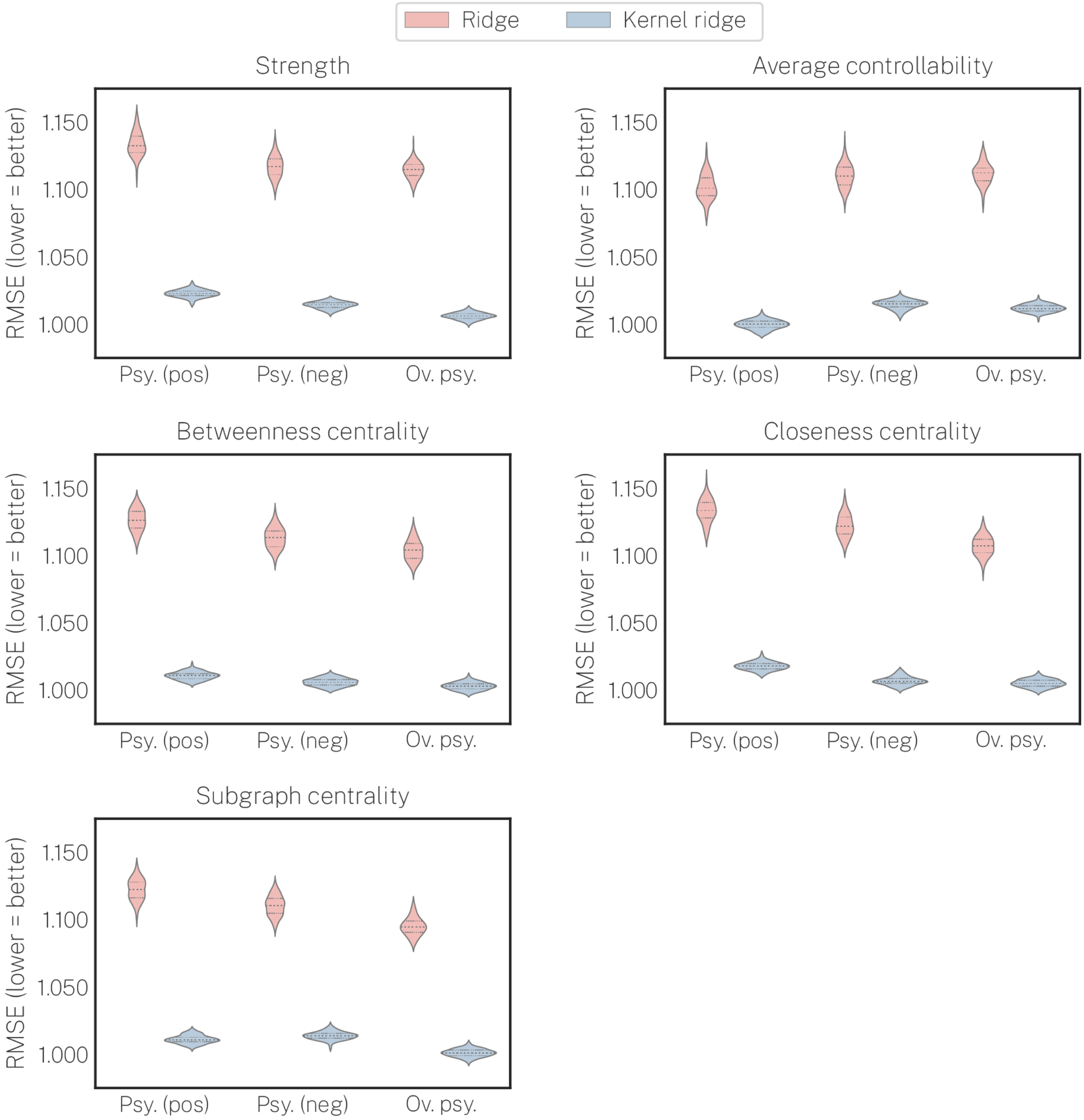

Figure S6. Nonlinear kernel ridge regression outperforms linear ridge regression at out-of-sample prediction of PS symptoms and overall psychopathology. Prediction performance, measured via root mean squared error (RMSE; lower = better), for each connectivity feature predicting each symptom dimension under our *primary prediction model*. For all connectivity features and all symptom dimensions, kernel ridge regression unambiguously outperformed ridge regression demonstrating that nonlinear regression functions better map the relationship between regional structural connectivity and symptoms.

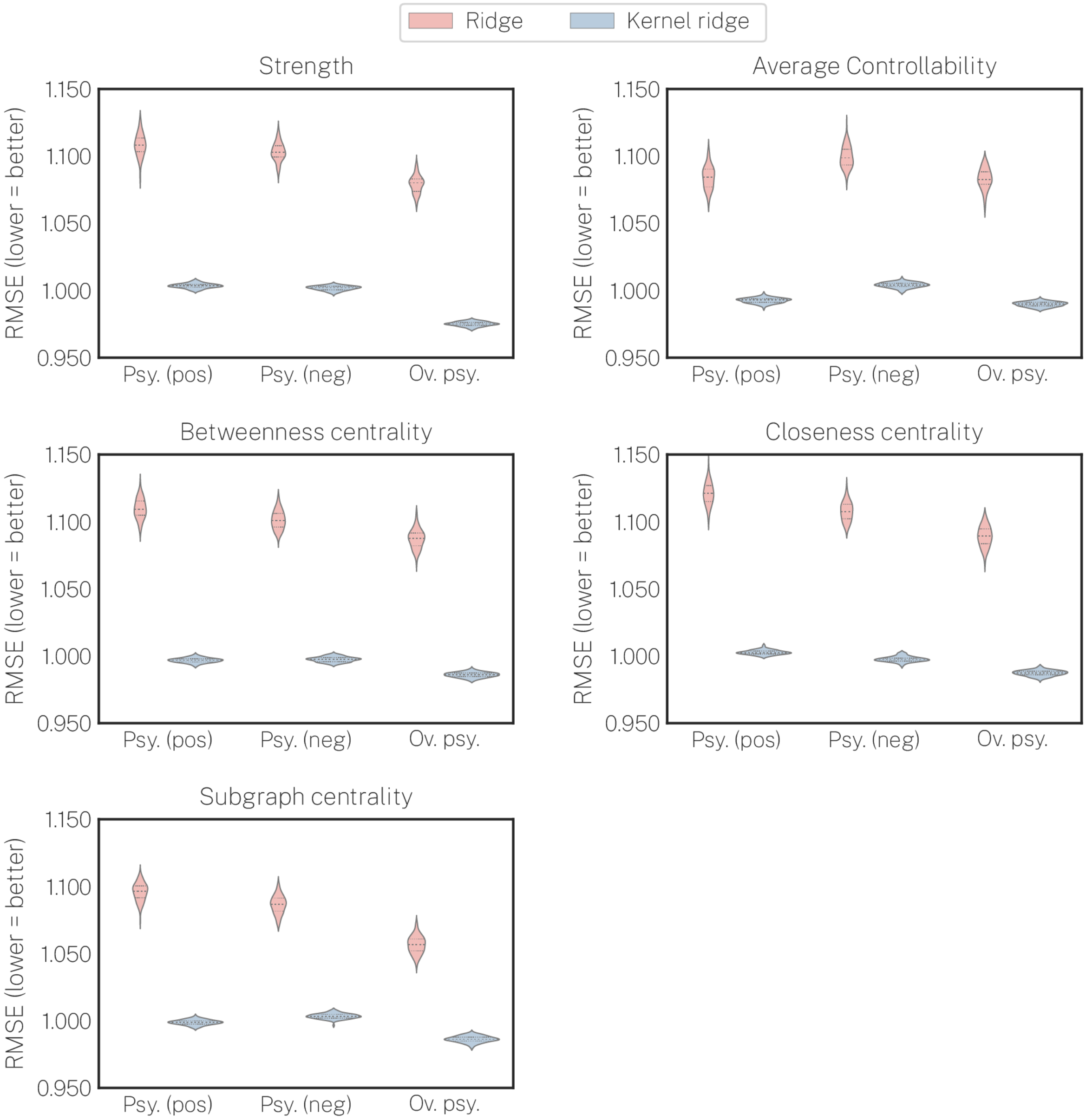

Figure S7. Nonlinear kernel ridge regression outperforms linear ridge regression at out-of-sample prediction under our *secondary prediction model*. Prediction performance, measured via root mean squared error (RMSE; lower = better), for each connectivity feature predicting each symptom dimension under our *secondary prediction model*. For all connectivity features and all symptom dimensions, kernel ridge regression unambiguously outperformed ridge regression demonstrating that nonlinear regression functions better map the relationship between regional structural connectivity and symptoms.

Examining indirect regional structural connectivity with network control theory enables better prediction of positive psychosis spectrum symptoms

In the main text, we reported that average controllability was able to predict psychosis-positive scores beyond chance levels. Figure S8 illustrates prediction performance measured via RMSE (Figure S8A) and the correlation between true y and predicted y (Figure S8B) alongside the corresponding empirical nulls from our *null prediction model.*

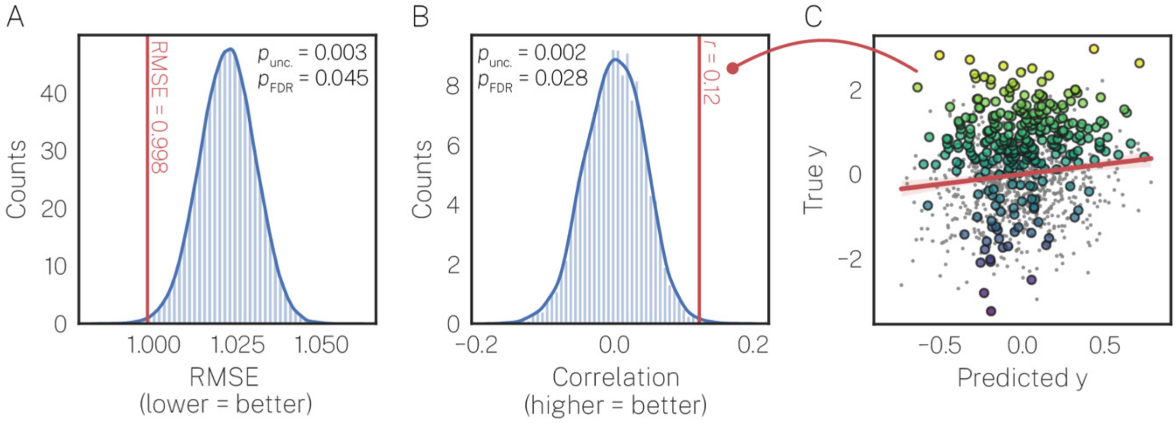

Figure S8. Empirical nulls for average controllability predicting psychosis-positive scores as well as a scatterplot depicting true versus predicted scores. A, Null observed for root mean squared error (RMSE; lower = better). **B**, Null observed for the correlation between true y and predicted y (higher = better). **C**, True versus predicted psychosis-positive scores (y). Individuals on the psychosis spectrum (n=303; see Table 1) are colored according to their psychosis-positive scores. The remainder of the cohort (n=765) are shown as smaller gray points.

In addition, we also retrained our model on the 303 individuals in our sample that expressed either subclinical or clinical PS symptoms (see Table 1 and Figure S4). These individuals are highlighted above in Figure S8C colored according their scores on the psychosis-positive dimension (mean and variance of psychosis-positive scores was 0.69 and 0.997 for these 303 individuals and -0.28 and 0.729 for the remaining individuals). In retraining our prediction model, we found prediction performance of RMSE = 0.992 and r = 0.16, which was slightly better than performance from the full cohort (see Figure S8). Finally, we also retrained our model on 100 subsets of 303 individuals randomly sampled (without replacement) from the full cohort. This process yielded prediction performance of RMSE = 1.004±0.032 and r = 0.04±0.07. This prediction performance was, on average, lower than performance from the full cohort and from the 303 PS individuals. We note, though, that performance was quite variable in this smaller subset. These results show that, compared to the rest of the PNC, PS individuals had positive symptoms that were better predicted from average controllability. Additionally, Figure S8C demonstrates that the 303 PS individuals were not unambiguously separable from the rest of the sample, instead appearing as an extreme extension of normative psychosis-positive scores. Thus, this data suggests that the psychosis-positive dimension is linked to abnormalities in average controllability that spans both those with PS symptoms and those without.

Comparison of prediction performance across connectivity features for each symptom dimension.

In Figure 2 in the main text, we reported the results of exact tests of differences that compared predictive performance from our *primary prediction model* (nuisance regression without hyper-parameter optimization) between pairs of connectivity features for each symptom dimension. Here, in Figure S9, we report the same set of analyses under our *secondary prediction model* (hyper-parameter optimization without nuisance regression).

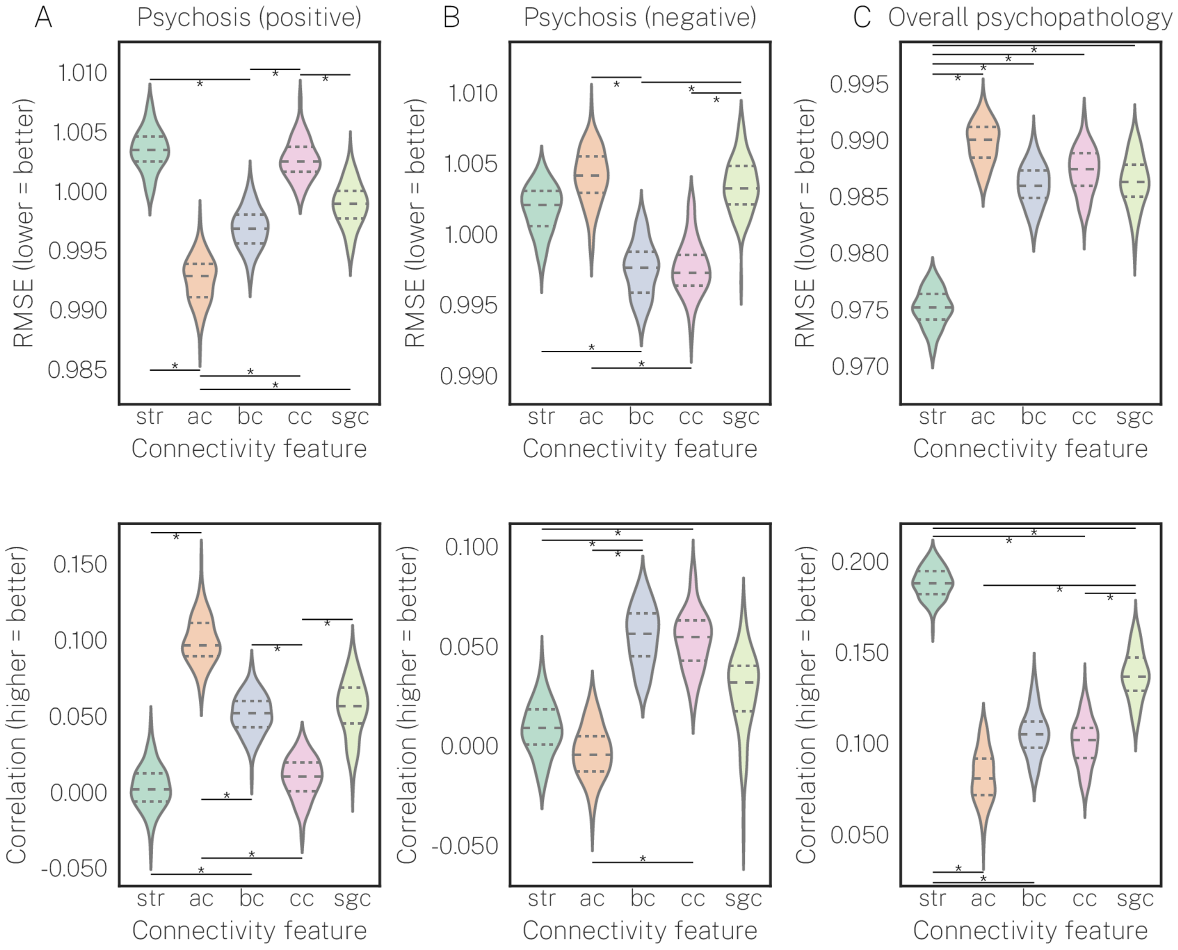

Figure S9. Prediction performance under our *secondary prediction model*. Each subplot shows prediction performance under our *secondary prediction model* using a nonlinear kernel ridge regression estimator. The top row indicates prediction performance measured via root mean squared error (RMSE; lower = better) and the bottom row indicates prediction performance measured via the correlation between true y and predicted y (higher = better). Note, that the high predictive performance observed between strength and overall psychopathology is due to the shared confound with age, which correlated strongly with both. str = strength. ac = average controllability. bc = betweenness centrality. cc = closeness centrality. sgc = subgraph centrality.

Spatial correlation between pairs of connectivity features

In the main text, we illustrated how the regional correlation between strength and average controllability varied as a function of the principal cortical gradient of functional connectivity (Figure 3A). Here, for completeness, we present this same effect for each pair of connectivity features studied herein (Figure S10). Note, *p*-values were assigned with the spin test (59–61), using 10,000 spins, and were corrected for multiple comparisons using FDR. Figure S10 shows that the spatial effect of the principal gradient was only significant for the strength versus average controllability correlation maps and betweenness versus closeness centrality correlation maps. These results suggest that the location along the gradient where metrics diverge depends upon the way in which they index connectivity. That is, the ways in which strength and average controllability index connectivity diverges most in transmodal cortex, while the ways in which betweenness and closeness centrality index connectivity diverges most in unimodal cortex.

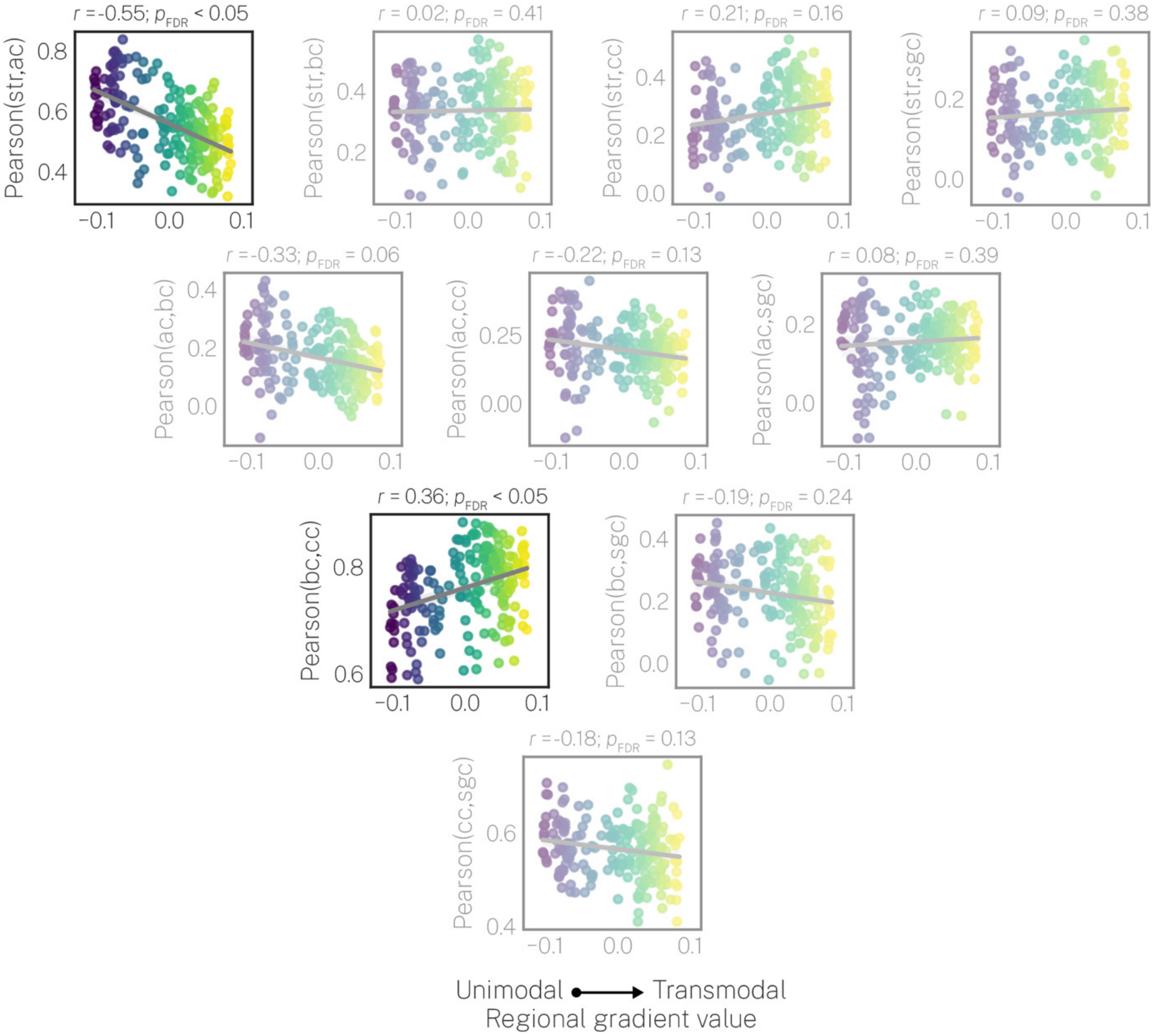

Figure S10. Regional correlations between pairs of connectivity features as a function of the principal cortical gradient. For completeness, results for strength versus average controllability are duplicated here from Figure 3. Non-significant effects are shown with increased transparency. str = strength. ac = average controllability. bc = betweenness centrality. cc = closeness centrality. sgc = subgraph centrality.

Extended results for binned-regions prediction model

In the main text we illustrated how prediction performance varied over the cortical gradient for psychosis-positive scores using our *binned-regions prediction model*. Here, for completeness, we show the same analysis for all combinations of connectivity features and symptom dimensions (Figure S11). Concerning strength and average controllability, no spatial effects of the cortical gradient were observed for strength predicting psychosis-negative and overall psychopathology, nor for average controllability predicting overall psychopathology. That is, prediction performance was uniform across the cortex. A small negative spatial effect was observed for average controllability predicting psychosis-negative, wherein regions in the transmodal cortex yielded slightly better predictive performance compared to regions in the unimodal cortex. Concerning our graph-theoretic measures of centrality, similar to strength, betweenness centrality did not reveal strong spatial effects of note. Closeness centrality revealed small positive spatial effects for all symptom dimensions, wherein regions in the unimodal cortex yielded better predictive performance compared to regions in the transmodal cortex. Conversely, subgraph centrality yielded negative spatial effects for psychosis-positive and psychosis-negative, but these were weaker than those observed for average controllability predicting psychosis-positive. These results demonstrate that the way in which indirect connections to a region are summarized may play an important role in the prediction of PS symptoms. In particular, it points to the intriguing possibility that prediction may be optimized by targeted selection of specific connectivity features at different ends of the cortical gradient (e.g., closeness centrality in unimodal regions and average controllability in transmodal regions). However, we are reluctant to interpret these effects as only the combination of average controllability and psychosis-positive yielded above-chance predictive performance.

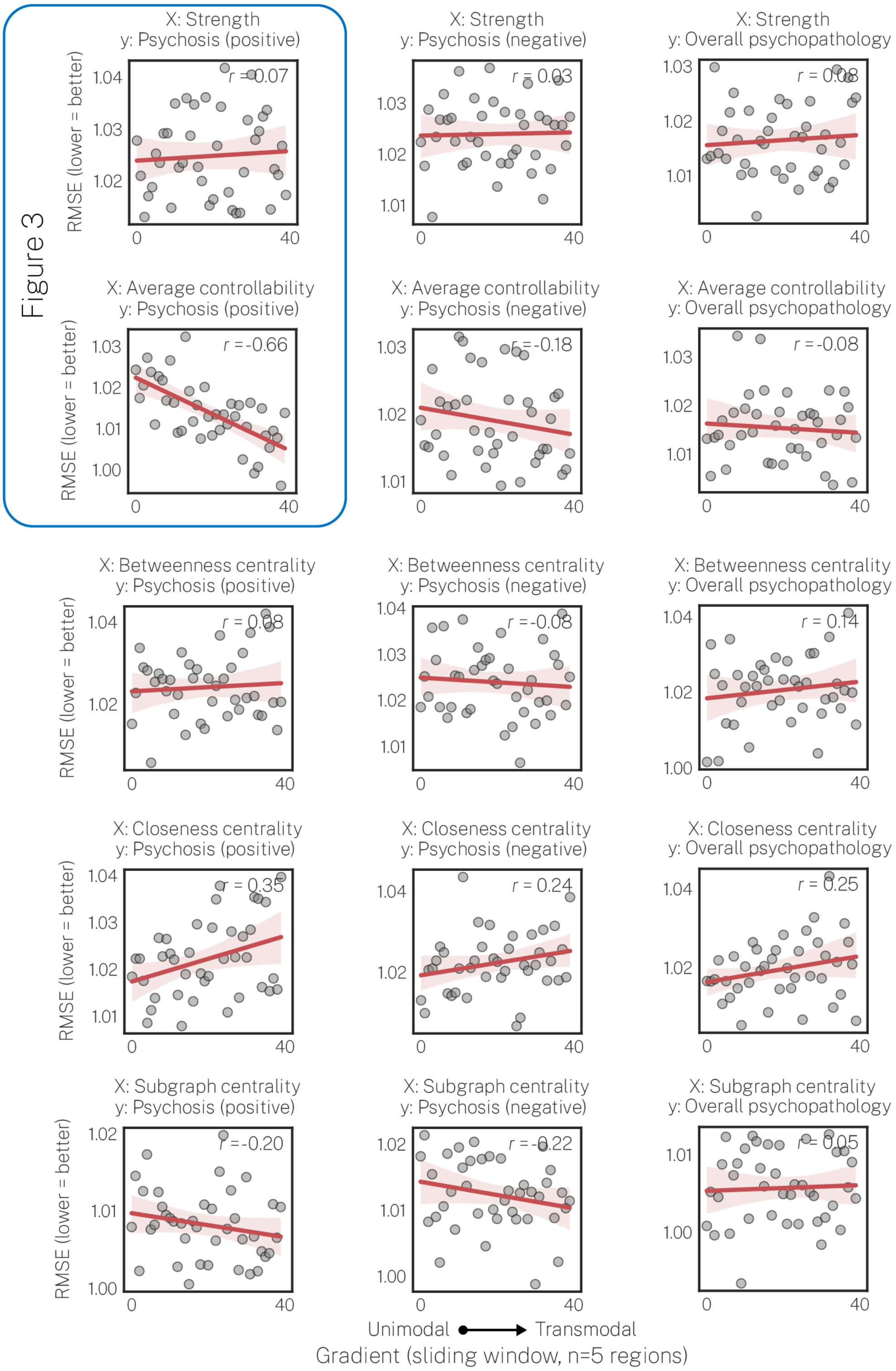

Figure S11. Prediction performance as a function of the cortical gradient for each combination of connectivity feature (X) and symptom dimension (y). For completeness, results for strength and average controllability predicting psychosis-positive scores are duplicated here from Figure 3. The strongest effect of the cortical gradient was observed for average controllability predicting psychosis-positive scores. Note that here no significance testing was conducted.

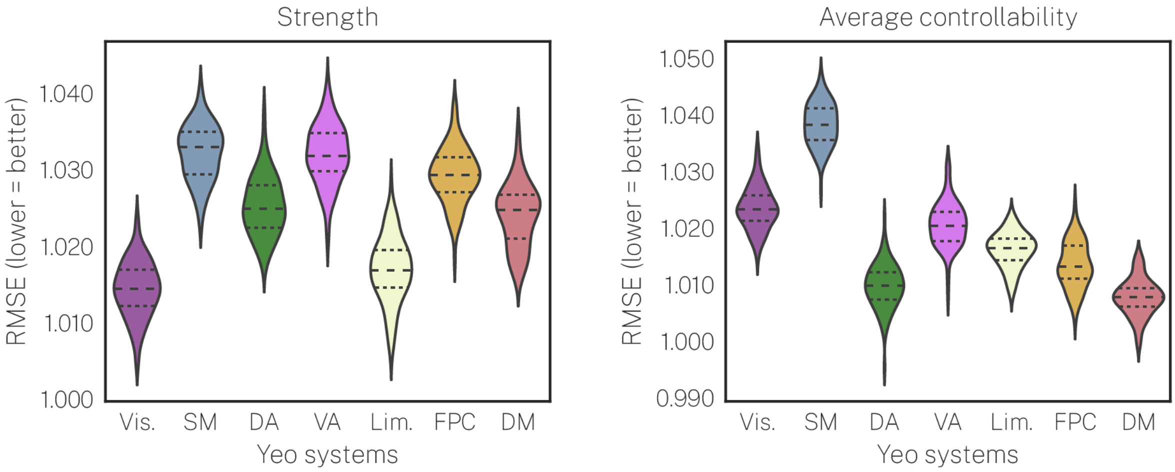

Figure S12. Prediction performance for psychosis-positive under our primary prediction model as a function of 7 Yeo systems. Prediction performance under our primary prediction model using a Kernel Ridge Regression estimator for strength (left) and average controllability (right) as a function of brain system. For each system, our primary prediction model was retrained using only regions from within that system. For strength, best prediction performance was observed for the visual and limbic systems. For average controllability, best prediction performance was observed for the dorsal attention and default mode systems. Vis. = visual. SM = somatomotor. DA = dorsal attention. VA = ventral attention. Lim. = limbic. FPC = frontoparietal control. DM = default mode.

Binned-regions prediction model: varying bin size

In the main text, we reported results for the *binned-regions prediction model* using bins of 5 regions sampled along the principal cortical gradient. Here, we aimed to replicate our *binned-regions prediction model* as a function of bin size. Table S3 shows that the negative correlation between bins of region and RMSE for average controllability predicting the psychosis-positive dimension was highly conserved across bin sizes, only breaking down for average controllability at bin sizes of ≤3.

Table S3. Pearson's correlation between out-of-sample RMSE and bins of regions sampled along the cortical gradient as a function of bin size.

	Bin size (number of regions)									
	1	2	3	4	5	6	7	8	9	10
Strength, *r*-value	0.07	0.09	0.13	-0.10	0.07	-0.02	0.03	-0.08	-0.15	-0.10
Average Controllability, *r*-value	-0.08	-0.01	-0.24	-0.60	-0.66	-0.59	-0.48	-0.59	-0.65	-0.70

Brain parcellation

In the main text, we reported results for the Schaefer200 parcellation. Here, we aimed to replicate our key results using the Schaefer400, Lausanne234, and HCP-MMP parcellations. Most pertinently, we examined (i) the extent to which our *primary prediction model* yielded improved prediction of psychosis-positive scores for average controllability relative to strength and (ii) whether the correlations between strength and average controllability varied over the principal cortical gradient (i.e., the effect reported in Figure 3A). Results for these analyses are presented below in Figure S13.

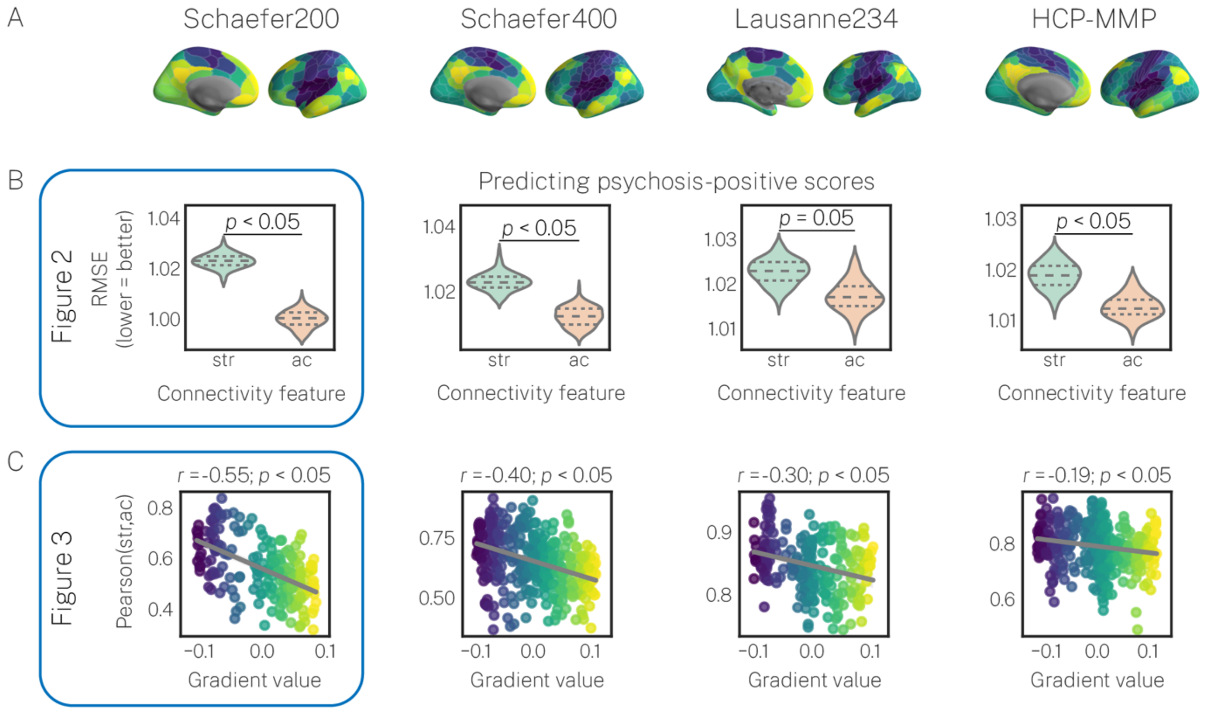

Figure S13. Predictive performance of psychosis-positive scores and cross-metric correlations as a function of brain parcellation. Each column represents one of four brain parcellations utilized in the current study, starting with the primary parcellation on the left (Schaefer200). **A**, The principal cortical gradient of functional connectivity for each brain parcellation. The gradient was highly conserved across parcellations. **B**, Predictive performance of strength and average controllability predicting psychosis-positive scores under our *primary prediction model*. For each parcellation, average controllability yielded significantly better predictive performance compared to strength. Improved prediction for average controllability was marginal for Lausanne234 ($p = 0.05$). **C**, Correlations between strength and average controllability as a function of the principal cortical gradient. The negative spatial effect of the gradient, wherein strength and average controllability diverge most in transmodal cortex, was conserved across parcellations. For completeness, results from Figures 2 and 3 are duplicated here. str = strength. ac = average controllability.

Figure S13 shows that our results are broadly reproduced across parcellations. First, under our *primary prediction model*, average controllability better predicted psychosis-positive scores when compared to strength (Figure S13B). This effect was significant for all parcellations except for Lausanne234, which was marginal at $p = 0.05$.

Next, Figure S13C shows that the negative spatial effect on the link between strength and average controllability was conserved across parcellations. Thus, the observation that average controllability indexes increasingly unique inter-individual variation at the top end of the cortical gradient was upheld.

Extended analysis of the effect of age

In the main text, we controlled for the effects of age in all of our prediction analyses. However, as mentioned in the introduction of the main text, previous literature has demonstrated that age is a key factor in the emergence of both PS symptoms and associated dysconnectivity throughout youth (62,63). Thus, here we sought to characterize the effect of age on our analyses by repeating our prediction models using a mean split approach. Specifically, we split our sample of n=1,068 individuals into two groups, one of n=539 individuals (age_{low}) who were all younger than the mean age of our sample (15 years) and a second of n=529 individuals (age_{high}) who were all older than the mean age. Next, in each age group (age_{low}, age_{high}) we examined the following: (i) whether the correlations between strength and average controllability varied over the principal cortical gradient (i.e., the effect reported in Figure 3A) and (ii) the extent to which prediction of psychosis-positive scores varied over the cortical gradient and was best in transmodal cortex (i.e., the effect reported in Figure 3B). Results for these analyses are presented below in Figure S14. Note, owing to the fact that our statistical power was cut in half, we did not test for significance of prediction here (i.e., under our *null prediction model*). Any loss of above-chance predictive performance here could not be rigorously distinguished from a simple consequence of lower statistical power.

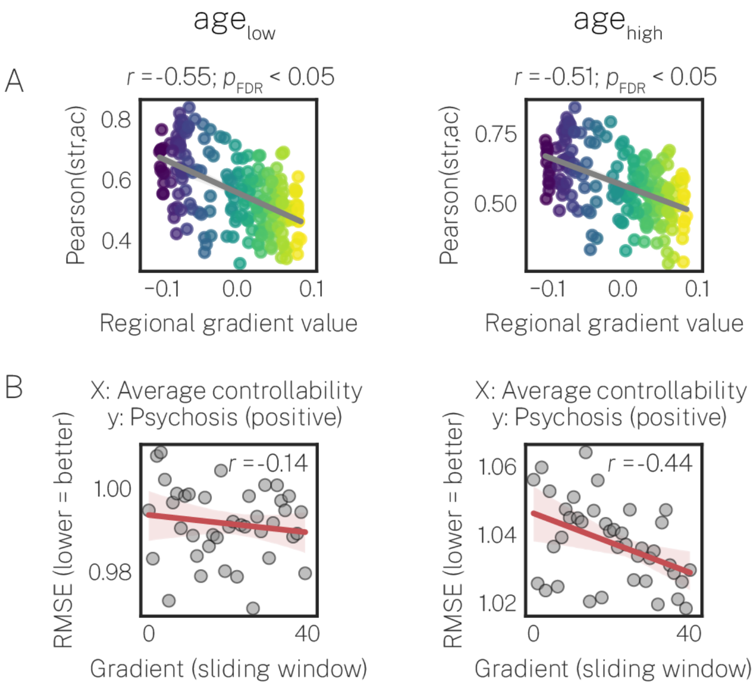

Figure S14. Correlations between strength and average controllability as well as results from our *binned-regions prediction* model after splitting the full sample into two subsamples based on age. Data from the full sample (n=1,068) were split into two subsamples at the mean age point (15 years). age_{low} (left) represents n=539 individuals that were younger than 15 years of age and age_{high} (right) represents n=529 individuals who were older than 15 years of age. **A**, Correlation between strength and average controllability as a function of the cortical gradient for age_{low} and age_{high}. **B**, Results from the *binned-regions prediction model* for age_{low} and age_{high}.

Figure S14 above shows that the effect of the cortical gradient on the correlation between strength and average controllability was virtually identical for both age_{low} and age_{high} (Figure S14A). By contrast results from our *binned-regions prediction model* showed that the spatial effect of the cortical gradient, wherein prediction was higher in transmodal cortex relative to unimodal cortex, was more pronounced in age_{high} compared to age_{low}. This distinction suggests that the dysconnectivity centered on transmodal cortex that predicts positive PS symptoms may be driven predominantly by individuals >15 years of age in our sample. This observation is consistent with previous literature positing that this period of mid adolescence coincides with the onset of psychotic disorders such as schizophrenia (62).

SUPPLEMENTARY REFERENCES

1. Satterthwaite TD, Elliott MA, Ruparel K, Loughead J, Prabhakaran K, Calkins ME, *et al.* (2014): Neuroimaging of the Philadelphia Neurodevelopmental Cohort. *NeuroImage* 86: 544–553.
2. Roalf DR, Quarmley M, Elliott MA, Satterthwaite TD, Vandekar SN, Ruparel K, *et al.* (2016): The impact of quality assurance assessment on diffusion tensor imaging outcomes in a large-scale population-based cohort. *NeuroImage* 125: 903–919.
3. Rosen AFG, Roalf DR, Ruparel K, Blake J, Seelaus K, Villa LP, *et al.* (2018): Quantitative assessment of structural image quality. *NeuroImage* 169: 407–418.
4. Tang E, Giusti C, Baum GL, Gu S, Pollock E, Kahn AE, *et al.* (2017): Developmental increases in white matter network controllability support a growing diversity of brain dynamics. *Nature Communications* 8. https://doi.org/10.1038/s41467-017-01254-4
5. Cornblath EJ, Tang E, Baum GL, Moore TM, Adebimpe A, Roalf DR, *et al.* (2019): Sex differences in network controllability as a predictor of executive function in youth. *NeuroImage* 188: 122–134.
6. Baum GL, Ciric R, Roalf DR, Betzel RF, Moore TM, Shinohara RT, *et al.* (2017): Modular Segregation of Structural Brain Networks Supports the Development of Executive Function in Youth. *Current Biology* 27: 1561-1572.e8.
7. Merikangas KR, Calkins ME, Burstein M, He J-P, Chiavacci R, Lateef T, *et al.* (2015): Comorbidity of Physical and Mental Disorders in the Neurodevelopmental Genomics Cohort Study. 135: 14.

8. Margulies DS, Ghosh SS, Goulas A, Falkiewicz M, Huntenburg JM, Langs G, *et al.* (2016): Situating the default-mode network along a principal gradient of macroscale cortical organization. *Proc Natl Acad Sci USA* 113: 12574–12579.
9. Parkes L, Tiego J, Aquino K, Braganza L, Chamberlain SR, Fontenelle LF, *et al.* (2019): Transdiagnostic variations in impulsivity and compulsivity in obsessive-compulsive disorder and gambling disorder correlate with effective connectivity in cortical-striatal-thalamic-cortical circuits. *NeuroImage* 202: 116070.
10. Cuthbert BN, Insel TR (2013): Toward the future of psychiatric diagnosis: the seven pillars of RDoC. *BMC Med* 11: 126.
11. Insel T, Cuthbert B, Garvey M, Heinssen R, Pine DS, Quinn K, *et al.* (2010): Research Domain Criteria (RDoC): Toward a New Classification Framework for Research on Mental Disorders. *AJP* 167: 748–751.
12. Kotov R, Krueger RF, Watson D, Achenbach TM, Althoff RR, Bagby RM, *et al.* (2017): The Hierarchical Taxonomy of Psychopathology (HiTOP): A dimensional alternative to traditional nosologies. *Journal of Abnormal Psychology* 126: 454–477.
13. Calkins ME, Moore TM, Merikangas KR, Burstein M, Satterthwaite TD, Bilker WB, *et al.* (2014): The psychosis spectrum in a young U.S. community sample: findings from the Philadelphia Neurodevelopmental Cohort. - 13: 296–305.
14. Calkins ME, Merikangas KR, Moore TM, Burstein M, Behr MA, Satterthwaite TD, *et al.* (2015): The Philadelphia Neurodevelopmental Cohort: constructing a deep phenotyping collaborative. *J Child Psychol Psychiatr* 56: 1356–1369.

15. Shanmugan S, Wolf DH, Calkins ME, Moore TM, Ruparel K, Hopson RD, *et al.* (2016): Common and Dissociable Mechanisms of Executive System Dysfunction Across Psychiatric Disorders in Youth. *American Journal of Psychiatry* 173: 517–526.
16. Kaczkurkin AN, Moore TM, Calkins ME, Ciric R, Detre JA, Elliott MA, *et al.* (2018): Common and dissociable regional cerebral blood flow differences associate with dimensions of psychopathology across categorical diagnoses. *Molecular Psychiatry* 23: 1981–1989.
17. Kaczkurkin AN, Park SS, Sotiras A, Moore TM, Calkins ME, Cieslak M, *et al.* (2019): Evidence for Dissociable Linkage of Dimensions of Psychopathology to Brain Structure in Youths. *AJP* appi.ajp.2019.1.
18. Merikangas KR, Avenevoli S, Costello EJ, Koretz D, Kessler RC (2009): National Comorbidity Survey Replication Adolescent Supplement (NCS-A): I. Background and Measures. *Journal of the American Academy of Child & Adolescent Psychiatry* 48: 367–379.
19. Sabaroedin K, Tiego J, Parkes L, Sforazzini F, Finlay A, Johnson B, *et al.* (2019): Functional Connectivity of Corticostriatal Circuitry and Psychosis-like Experiences in the General Community. *Biological Psychiatry* 86: 16–24.
20. McGlashan TH, Miller TJ, Woods SW, Rosen JL, Hoffman RE, Davidson L (2003): *Structured Interview for Prodromal Syndromes, Version 4.0.* New Haven, CT: Prime Clinical Yale School of Medicine.

21. Muthen LK, Muther BO (1998): *Mplus User's Guide*, 7th ed. Los Angeles, CA: Muthen & Muthen.
22. Owen MJ, Sawa A, Mortensen PB (2016): Schizophrenia. *The Lancet* 388: 86–97.
23. Satterthwaite TD, Elliott MA, Gerraty RT, Ruparel K, Loughead J, Calkins ME, *et al.* (2013): An improved framework for confound regression and filtering for control of motion artifact in the preprocessing of resting-state functional connectivity data. *NeuroImage* 64: 240–256.
24. Ciric R, Rosen AFG, Erus G, Cieslak M, Adebimpe A, Cook PA, *et al.* (2018): Mitigating head motion artifact in functional connectivity MRI. *Nat Protoc* 13: 2801–2826.
25. Tustison NJ, Cook PA, Klein A, Song G, Das SR, Duda JT, *et al.* (2014): Large-scale evaluation of ANTs and FreeSurfer cortical thickness measurements. *NeuroImage* 99: 166–179.
26. Avants BB, Tustison NJ, Song G, Cook PA, Klein A, Gee JC (2011): A reproducible evaluation of ANTs similarity metric performance in brain image registration. *NeuroImage* 54: 2033–2044.
27. Tustison NJ, Avants BB, Cook PA, Yuanjie Zheng, Egan A, Yushkevich PA, Gee JC (2010): N4ITK: Improved N3 Bias Correction. *IEEE Trans Med Imaging* 29: 1310–1320.
28. Avants BB, Tustison NJ, Wu J, Cook PA, Gee JC (2011): An Open Source Multivariate Framework for n-Tissue Segmentation with Evaluation on Public Data. *Neuroinform* 9: 381–400.

29. Klein A, Ghosh SS, Avants B, Yeo BTT, Fischl B, Ardekani B, *et al.* (2010): Evaluation of volume-based and surface-based brain image registration methods. *NeuroImage* 51: 214–220.

30. Jenkinson M, Bannister P, Brady M, Smith S (2002): Improved Optimization for the Robust and Accurate Linear Registration and Motion Correction of Brain Images. *NeuroImage* 17: 825–841.

31. Andersson JLR, Sotiropoulos SN (2016): An integrated approach to correction for off-resonance effects and subject movement in diffusion MR imaging. *NeuroImage* 125: 1063–1078.

32. Jenkinson M, Beckmann CF, Behrens TEJ, Woolrich MW, Smith SM (2012): FSL. *NeuroImage* 62: 782–790.

33. Yeh F-C, Verstynen TD, Wang Y, Fernández-Miranda JC, Tseng W-YI (2013): Deterministic Diffusion Fiber Tracking Improved by Quantitative Anisotropy ((W. Zhan, editor)). *PLoS ONE* 8: e80713.

34. Calabrese E, Badea A, Cofer G, Qi Y, Johnson GA (2015): A Diffusion MRI Tractography Connectome of the Mouse Brain and Comparison with Neuronal Tracer Data. *Cereb Cortex* 25: 4628–4637.

35. Dauguet J, Peled S, Berezovskii V, Delzescaux T, Warfield SK, Born R, Westin C-F (2007): Comparison of fiber tracts derived from in-vivo DTI tractography with 3D histological neural tract tracer reconstruction on a macaque brain. *NeuroImage* 37: 530–538.

36. Kim JZ, Soffer JM, Kahn AE, Vettel JM, Pasqualetti F, Bassett DS (2018): Role of graph architecture in controlling dynamical networks with applications to neural systems. *Nature Phys* 14: 91–98.
37. Seguin C, Tian Y, Zalesky A (2020): *Network Communication Models Improve the Behavioral and Functional Predictive Utility of the Human Structural Connectome*. Neuroscience. https://doi.org/10.1101/2020.04.21.053702
38. van den Heuvel MP, de Reus MA, Feldman Barrett L, Scholtens LH, Coopmans FMT, Schmidt R, *et al.* (2015): Comparison of diffusion tractography and tract-tracing measures of connectivity strength in rhesus macaque connectome: Comparison of Diffusion Tractography and Tract-Tracing Measures. *Hum Brain Mapp* 36: 3064–3075.
39. Delettre C, Messé A, Dell L-A, Foubet O, Heuer K, Larrat B, *et al.* (2019): Comparison between diffusion MRI tractography and histological tract-tracing of cortico-cortical structural connectivity in the ferret brain. *Network Neuroscience* 3: 1038–1050.
40. Saleeba C, Dempsey B, Le S, Goodchild A, McMullan S (2019): A Student’s Guide to Neural Circuit Tracing. *Front Neurosci* 13: 897.
41. Parkes L, Fulcher B, Yücel M, Fornito A (2018): An evaluation of the efficacy, reliability, and sensitivity of motion correction strategies for resting-state functional MRI. *NeuroImage* 171: 415–436.

42. Smith SM, Jenkinson M, Woolrich MW, Beckmann CF, Behrens TEJ, Johansen-Berg H, *et al.* (2004): Advances in functional and structural MR image analysis and implementation as FSL. *NeuroImage* 23: S208–S219.

43. Cox RW (1996): AFNI: Software for Analysis and Visualization of Functional Magnetic Resonance Neuroimages. *Computers and Biomedical Research* 29: 162–173.

44. Ciric R, Wolf DH, Power JD, Roalf DR, Baum GL, Ruparel K, *et al.* (2017): Benchmarking of participant-level confound regression strategies for the control of motion artifact in studies of functional connectivity. *NeuroImage* 154: 174–187.

45. Hallquist MN, Hwang K, Luna B (2013): The nuisance of nuisance regression: Spectral misspecification in a common approach to resting-state fMRI preprocessing reintroduces noise and obscures functional connectivity. *NeuroImage* 82: 208–225.

46. Schaefer A, Kong R, Gordon EM, Laumann TO, Zuo X-N, Holmes AJ, *et al.* (2018): Local-Global Parcellation of the Human Cerebral Cortex from Intrinsic Functional Connectivity MRI. *Cerebral Cortex* 28: 3095–3114.

47. Baum GL, Cui Z, Roalf DR, Ciric R, Betzel RF, Larsen B, *et al.* (2020): Development of structure–function coupling in human brain networks during youth. *Proc Natl Acad Sci USA* 117: 771–778.

48. Daducci A, Gerhard S, Griffa A, Lemkaddem A, Cammoun L, Gigandet X, *et al.* (2012): The Connectome Mapper: An Open-Source Processing Pipeline to Map Connectomes with MRI ((C. P. Hess, editor)). *PLoS ONE* 7: e48121.

49. Glasser MF, Coalson TS, Robinson EC, Hacker CD, Harwell J, Yacoub E, *et al.* (2016): A multi-modal parcellation of human cerebral cortex. *Nature* 536: 171–178.
50. Oldham S, Fulcher B, Parkes L, Arnatkevic̆iūtė A, Suo C, Fornito A (2019): Consistency and differences between centrality measures across distinct classes of networks ((S. Hayasaka, editor)). *PLoS ONE* 14: e0220061.
51. Murphy KP (2012): *Machine Learning: A Probabilistic Perspective*. Cambridge, MA: MIT Press.
52. Pedregosa F, Varoquaux G, Gramfort A, Michel V, Thirion B, Grisel O, *et al.* (n.d.): Scikit-learn: Machine Learning in Python. *MACHINE LEARNING IN PYTHON* 6.
53. Varoquaux G, Raamana PR, Engemann DA, Hoyos-Idrobo A, Schwartz Y, Thirion B (2017): Assessing and tuning brain decoders: Cross-validation, caveats, and guidelines. *NeuroImage* 145: 166–179.
54. MacKinnon JG (2009): Bootstrap Hypothesis Testing. In: Belsley DA, Kontoghiorghes EJ, editors. *Handbook of Computational Econometrics*. Chichester, UK: John Wiley & Sons, Ltd, pp 183–213.
55. Poldrack RA, Huckins G, Varoquaux G (2019): Establishment of Best Practices for Evidence for Prediction: A Review. *JAMA Psychiatry*. https://doi.org/10.1001/jamapsychiatry.2019.3671
56. Benjamini Y, Hochberg Y (1995): Controlling the False Discovery Rate: A Practical and Powerful Approach to Multiple Testing. *Journal of the Royal Statistical Society: Series B (Methodological)* 57: 289–300.

57. Vos de Wael R, Benkarim O, Paquola C, Lariviere S, Royer J, Tavakol S, *et al.* (2020): BrainSpace: a toolbox for the analysis of macroscale gradients in neuroimaging and connectomics datasets. *Commun Biol* 3: 103.
58. Karrer TM, Kim JZ, Stiso J, Kahn AE, Pasqualetti F, Habel U, Bassett DS (2020): A practical guide to methodological considerations in the controllability of structural brain networks. *J Neural Eng* 17: 026031.
59. Váša F, Seidlitz J, Romero-Garcia R, Whitaker KJ, Rosenthal G, Vértes PE, *et al.* (2018): Adolescent Tuning of Association Cortex in Human Structural Brain Networks. *Cerebral Cortex* 28: 281–294.
60. Alexander-Bloch A, Raznahan A, Bullmore E, Giedd J (2013): The Convergence of Maturational Change and Structural Covariance in Human Cortical Networks. *Journal of Neuroscience* 33: 2889–2899.
61. Alexander-Bloch AF, Shou H, Liu S, Satterthwaite TD, Glahn DC, Shinohara RT, *et al.* (2018): On testing for spatial correspondence between maps of human brain structure and function. *NeuroImage* 178: 540–551.
62. Paus T, Keshavan M, Giedd JN (2008): Why do many psychiatric disorders emerge during adolescence? *Nat Rev Neurosci* 9: 947–957.
63. Nath M, Wong TP, Srivastava LK (2021): Neurodevelopmental insights into circuit dysconnectivity in schizophrenia. *Progress in Neuro-Psychopharmacology and Biological Psychiatry* 104: 110047.